Upper-Ocean Processes and Sea Ice Production in the Southeastern Amundsen Sea Polynya in Austral Autumn

YIXI ZHENG,[a] BENJAMIN G. M. WEBBER,[a] KAREN J. HEYWOOD,[a] DAVID P. STEVENS,[b]
SHARON E. STAMMERJOHN,[c] AND ROB A. HALL[a]

[a] *Centre for Ocean and Atmospheric Sciences, School of Environmental Sciences, University of East Anglia, Norwich, Norfolk, United Kingdom*
[b] *Centre for Ocean and Atmospheric Sciences, School of Mathematics, University of East Anglia, Norwich, Norfolk, United Kingdom*
[c] *Institute of Arctic and Alpine Research, University of Colorado Boulder, Boulder, Colorado*

(Manuscript received 11 January 2024, in final form 1 October 2024, accepted 28 November 2024)

ABSTRACT: The mixed layer of polynyas is vital for local climate as it determines the exchange of properties and energy between ocean, sea ice, and atmosphere. However, its evolution is poorly understood, as it is controlled by complex interactions among these components, yet highly undersampled, especially outside summer. Here, we present a 2-month, high vertical-resolution, full-depth hydrographic dataset from the southeastern Amundsen Sea polynya in austral autumn (from mid-February to mid-April 2014) collected by a recovered seal tag. This novel dataset quantifies the changes in upper-ocean temperature and salinity stratification in this previously unobserved season. Our seal-tag measurements reveal that the mixed layer experiences deepening, salinification, and intense heat loss through surface fluxes. Heat and salt budgets suggest a sea ice formation rate of ~3 cm per day. We use a one-dimensional model to reproduce the mixed layer evolution and further identify key controls on its characteristics. Our experiments with a range of reduced or amplified air–sea fluxes show that heat loss to the atmosphere and related sea ice formation are the principal determinants of stratification evolution. Additionally, our modeling demonstrates that horizontal advection is required to fully explain the mixed layer evolution, underlining the importance of the ice-covered neighboring region for determining sea ice formation rates in the Amundsen Sea polynya. Our findings suggest that the potential overestimation of sea ice production by satellite-based methods, due to the absence of oceanic heat flux, could be offset by horizontal advection inhibiting mixed layer deepening and sustaining sea ice formation.

KEYWORDS: Antarctica; Sea ice; Oceanic mixed layer; Heat budgets/fluxes; Salinity

1. Introduction

The interactions between the ocean, atmosphere, and cryosphere in polar regions are critical for the climate system. Understanding the processes driving these interactions is important in order to reduce uncertainties in projections of future climate and sea level rise. Our understanding is limited by a lack of observations, particularly in winter when the polar regions are more inaccessible and infrequently sampled. The areas of water open to intense heat loss to the cold atmosphere, such as polynyas, host higher sea ice production than ice-covered regions (Tamura et al. 2008). This has been attributed to intense heat loss to the atmosphere in these open-ocean areas and the fact that open ocean and thin sea ice allow one to two orders of magnitude more heat to be lost to the atmosphere than thick ice (Maykut 1982, 1978).

Among all Antarctic coastal polynyas, the Amundsen Sea polynya (ASP) is the fourth largest (Macdonald et al. 2023). Due to its proximity to some of the most rapidly melting ice shelves, the ASP has been an important site for oceanographic research (Yang et al. 2022; Kim et al. 2016; Randall-Goodwin et al. 2015). The ASP also has the highest primary productivity among Antarctic coastal polynyas, giving it key significance in biological activity and carbon uptake (Arrigo et al. 2012; Yager et al. 2012).

Previous research has focused on obtaining sea ice production rates from satellite microwave products (Tamura et al. 2016; Nihashi et al. 2017), which assumes that all the heat loss/gain from the atmosphere is used for sea ice formation/melting, and has a negligible effect on the heat content of the upper ocean. These assumptions are based predominantly on observations from cold shelf seas, revealing that the whole water column is near freezing during winter sea ice formation due to the frequent occurrence of deep convection (Jacobs and Giulivi 1985). However, these assumptions may not be applicable in relatively warm Antarctic shelf seas such as the Amundsen Sea, where modified Circumpolar Deep Water (mCDW) is present everywhere deeper than 400 m. As the mixed layer deepens, mCDW is constantly entrained into the upper ocean, providing heat to the mixed layer that eventually regulates sea ice formation from below the sea surface (Martinson 1990; Saenz et al. 2023; Ackley et al. 2015). Furthermore, due to ice

---

Denotes content that is immediately available upon publication as open access.

Supplemental information related to this paper is available at the Journals Online website: https://doi.org/10.1175/JPO-D-24-0006.s1.

Corresponding author: Yixi Zheng, yixi.zheng@uea.ac.uk

DOI: 10.1175/JPO-D-24-0006.1

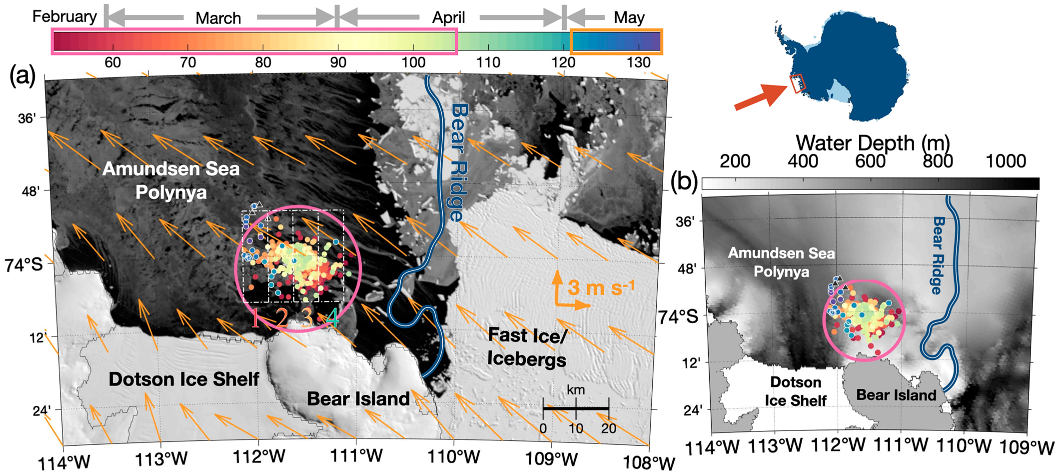

FIG. 1. Map of the southeastern Amundsen Sea. (a) Ice photography (MODIS *Terra* on 14 Mar 2014) overlaid by locations of EM959 seal-tag profiles, colored by yearday of data collection in 2014. Profiles used to analyze temporal variation in Figs. 4 and 5 are indicated by solid dots outlined by the pink circle in the map, with their data-collection yearday marked by a pink rectangle in the color bar. Dots with white edges indicate supplementary profiles collected from 1 to 13 May 2014 (from MEOP), with their data-collection yearday marked by the orange rectangle in the color bar. Black triangles with white edges indicate the profiles collected on 1 Sep 2014 (from MEOP). The curvy white-blue line shows schematically the shape of Bear Ridge [modified from Bett et al. (2020)]. Orange arrows show averaged wind speed and direction during the *EM959* measuring period. The dashed white boxes mark the four ERA5 grid points we use to area average the ERA5 reanalysis. (b) As in (a), but for bathymetry. The location of the study region in Antarctica is shown in the inset.

shelf basal melting, glacial-meltwater-rich water, that is warmer and fresher than the ambient Winter Water, is injected into the upper ocean and provides extra heat to the mixed layer that further moderates sea ice formation (Mankoff et al. 2012; Jourdain et al. 2017; Zheng et al. 2021). Hence, for warm Antarctic shelf seas, understanding the upper-ocean property evolution is crucial for obtaining a reliable sea ice production rate. The Amundsen Sea hosts several ice shelves vulnerable to basal melting. Sea ice production plays a vital role in controlling the mixed layer deepening, in turn affecting the heat transport into the ice shelf cavities, which contributes to ice shelf mass loss (Webber et al. 2017). Here, we derive and discuss the sea ice production rate in the Amundsen Sea.

Despite the importance of sea ice formation processes in the ASP, acquiring the related observations is extremely challenging. Although moorings have been deployed across the Amundsen Sea (Yang et al. 2022), to avoid snagging by icebergs, they rarely have sensors above 200 m, so are not able to resolve upper-ocean polynya processes. The deployment of seal tags greatly increases the amount of nonsummer season observations and allows us to study the transition from summer to winter. Nevertheless, due to the foraging and migration behavior of tagged seals, it is rare to obtain a seal-tag time series from one location. This study is based upon a fortuitous tag recovery that provides an unprecedented dataset in one location in the southeastern ASP, revealing the ocean conditions at high vertical- and temporal-resolution including the rarely observed near-surface layer during sea ice formation.

2. Data and methods

a. *Hydrographic observations from the southeastern ASP*

1) HIGH-RESOLUTION PROFILES FROM A RECOVERED SEAL TAG, *EM959*

In February 2014, a seal-tagging team onboard the RRS *James Clark Ross*, under the Ocean2ice project of the U.K.'s Ice Sheet Stability programme (Heywood et al. 2014), tagged a male southern elephant seal (tag serial number: EM959; hereafter, *EM959* for this tag). *EM959* was initially deployed on the Edwards Islands in Pine Island Bay, after which the instrumented seal moved west along the edge of the fast ice and grounded icebergs. This seal stayed in the southeastern corner of the Amundsen Sea polynya from mid-February to mid-April (yearday 51.8–105.7, Fig. 1). Thus, *EM959* measured the upper-ocean properties of the ASP continually for more than 2 months during austral autumn. *EM959* stopped working on 22 April while still attached to the seal's head. When the seal returned to Edwards Islands and moulted in late 2014, *EM959* remained on the beach until it was serendipitously found in 2020, by another seal-tagging team onboard the RV *Nathaniel B. Palmer*, part of the International Thwaites Glacier Collaboration (ITGC).

Seal tags typically include a small conductivity–temperature–depth (CTD) sensor recording in situ measurements every second (Boehme et al. 2009). However, to reduce data transmission and to extend the battery life of the tag, different algorithms are applied to select a range of about 18 depths from the deepest dive in every 4–6-h period. Only the measurements from those selected depths and dives are transmitted to the data center via the Argos satellite system (Boehme et al. 2009; Fedak et al. 2002; Fedak 2004; Photopoulou et al. 2015). The 1-s resolution time series is stored on the tag but is not usually obtained, since tags fall off during the seals' spring/summer moult and usually are lost. For reference, in 2014, *EM959* only transmitted 89 profiles via the Argos satellite system, with 18 depths in each profile; from the recovered tag, 513 profiles with up to 2079 depths per profile were obtained.

We calibrated *EM959* conductivity data against nearby ship-based CTD profiles (i.e., the seven CTD casts within 10 km and 5 days of *EM959* observations) obtained on the U.K.'s Ice Sheet Stability programme (iSTAR)/Ocean2ice cruise in the Amundsen Sea in February 2014 (Heywood et al. 2016). To include a relatively stable layer of conductivity values in the calibration, we chose profiles that encompassed the modified Circumpolar Deep Water, i.e., we chose seal profiles with a maximum Conservative Temperature > 0°C and extending below the pycnocline (depth > 800 m) and compared them with the closest CTD profile. We obtain one scaling factor for conductivity for each seal profile and then calculate the median scaling factor of 1.0018 ± 0.002, which is then applied to all seal profiles (Fig. S1 in the online supplemental material). We did not find a trend in the scaling factors in space or time. For all data used in this study, we follow the Thermodynamic Equation of Seawater-10 (TEOS-10; McDougall and Barker 2011) unless otherwise stated. Outliers were removed from the seal-tag hydrographic profiles following visual inspection. All seal-tag profiles discussed in this paper are at their full 1-s resolution (i.e., not binned spatially or temporally) unless otherwise stated.

In the following analysis, we only consider profiles collected when the instrumented seal was located within the pink circle in Fig. 1. The median distance from the locations of profiles to the center of our data collection region (center of the pink circle in Fig. 1; 74.017°S, 111.569°W) is 5.2 km. The baroclinic Rossby radius at this location is about 5 km, following the calculation described by Chelton et al. (1998). We assume that the spatial variation within this relatively small region is negligible compared with the temporal variation in our dataset. The dataset collected is thus considered a virtual mooring. We test this assumption by dividing the dataset into four quadrants relative to the center of the study area and find the temporal variability is much larger than the spatial variability of the upper-ocean processes (Fig. S2).

2) DATA COLLECTED FROM OTHER SEAL TAGS IN THE SAME YEAR

To extend the temporal coverage of the *EM959* dataset, we include 25 profiles from the same general location, but acquired later in the same year by three additional seal tags deployed on different seals during the same field campaign (Fig. 1a, dots and triangles with white edges). These 25 profiles were processed and quality controlled by Marine Mammals Exploring the Oceans Pole to Pole (MEOP; Roquet et al. 2013, 2014; http://www.meop.net), with 22 profiles obtained during 1–13 May 2014 and three profiles on 1 September 2014. Profiles from MEOP were calibrated against historical CTDs or by cross calibration between different seal tags. We further compare the *EM959* measurements calibrated using our methods as described in section 2a(1) with those postprocessed by MEOP and find the differences between them negligible: below 400 m, where the water mass has relatively stable properties, the mean values from our high-frequency observations and MEOP were −0.834° and −0.831°C for Conservative Temperature and 34.497 and 34.502 g kg^{-1} for Absolute Salinity, respectively. The calibrated measurements have uncertainties of ±0.03°C for temperature and ±0.05 g kg^{-1} for salinity. These MEOP profiles have measurements of salinity and temperature at 18 depths, including near-surface (2 dbar), temperature minimum (Winter Water core), deep (>100 m) temperature maximum (mCDW core), and the maximum dive depth, plus 14 other depths equally spaced between the sea surface and the maximum depth.

b. *Atmospheric reanalysis from ERA5*

We use hourly ERA5 reanalysis time series (Hersbach et al. 2020), including 2-m air temperature, 10-m wind stress, downward longwave radiation, downward shortwave radiation, precipitation, and specific humidity (not shown) to estimate air–sea fluxes (Fig. 2). All terms are defined as positive downward, i.e., positive when the ocean is gaining heat or freshwater from the atmosphere (Fig. 2).

We use bulk formulas to calculate air–sea fluxes. The use of bulk formulas is a common approach in ocean modeling (e.g., Griffies et al. 2016; Biddle et al. 2017; Wilson et al. 2019). The calculation of turbulent heat fluxes requires accurate sea surface temperature, which is more reliably represented by our seal-tag measurements than by the ERA5 reanalysis. Moreover, ERA5 provides positive sensible heat flux values after late March, likely due to the incorrect simulation of thick sea ice cover at this time, leading to a surface temperature lower than the air temperature. However, when thick ice is present, air–sea heat fluxes are significantly reduced, meaning that the actual sensible heat flux experienced by the ocean would be much lower than the atmospheric fluxes provided by ERA5. Therefore, using ERA5's positive sensible heat flux in our study would be less accurate than using our calculated fluxes. We hence use calculated turbulent heat fluxes rather than the fluxes available in ERA5. For reference, the net heat flux from ERA5 is 33.47 W m^{-2} higher than the net heat flux calculated using our bulk formula, likely due to ERA5's predicted sea ice cover reducing the air–sea heat fluxes. However, this difference does not qualitatively affect our results (Fig. S3).

Wind forcing contributes to upper-ocean changes, as its variability dominates the net heat fluxes, rather than other factors such as sea surface temperature (Fig. S4). We acknowledge that the air–sea drag coefficient is nonlinearly dependent on wind speed, sea ice concentration, and type (e.g., Elvidge et al. 2016), whereas we assume a constant drag coefficient, which further induces uncertainties in the air–sea fluxes. To account for the uncertainty involved in the assumption of constant

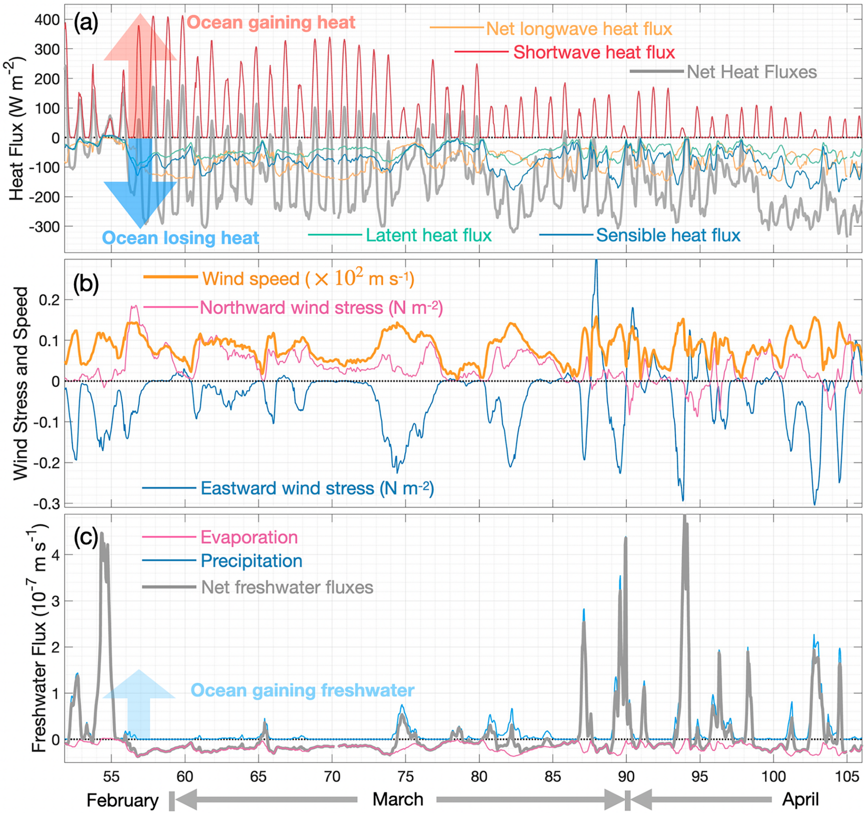

FIG. 2. Time series of fluxes. All fluxes are calculated using the ERA5 reanalysis and *EM959* observations (see section 2b for details). (a) Heat fluxes. Orange and red lines indicate the net longwave and downward shortwave radiations, respectively; and blue and green lines indicate the sensible and latent heat fluxes, respectively. The thick gray line indicates the net heat flux. (b) Momentum fluxes. Thin pink and blue lines indicate the 10-m wind stress in northward and eastward directions. The orange thick line indicates the 10-m wind speed. (c) Freshwater flux. Pink and blue lines indicate the evaporation and precipitation, respectively. The thick gray line indicates the net freshwater flux.

drag, we test the upper-ocean response to a range of heat and momentum fluxes, as discussed in section 4.

The net downward heat flux Q_{net} is given by

$$Q_{\mathrm{net}} = -(Q^{\mathrm{net}}_{\mathrm{longwave}} + Q_{\mathrm{sensible}} + Q_{\mathrm{latent}}) + Q^{\mathrm{downword}}_{\mathrm{shortwave}}, \qquad (1)$$

where $Q^{\mathrm{net}}_{\mathrm{longwave}}$ is the net longwave radiative flux. As upward longwave radiation depends upon sea surface temperature, we calculate $Q^{\mathrm{net}}_{\mathrm{longwave}}$ from sea surface temperature measured by *EM959* using Eq. (2).

$$Q^{\mathrm{net}}_{\mathrm{longwave}} = -\epsilon_{\mathrm{longwave}}\sigma \times (\mathrm{SST} + 273.15)^4 + \epsilon_{\mathrm{longwave}} Q^{\mathrm{downwards}}_{\mathrm{longwave}}, \qquad (2)$$

where $\sigma = 5.67 \times 10^{-8}$ W m^{-2} K^{-4} is the Stefan–Boltzmann constant, SST is the *EM959* sea surface temperature (in °C and depth-averaged over the top 3 m) interpolated to the ERA5 time steps, $\epsilon_{\mathrm{longwave}} = 0.97$ is the longwave emissivity of water (the absorptivity is assumed to have the same value), and $Q^{\mathrm{downward}}_{\mathrm{longwave}}$ is the downward longwave radiation from ERA5. The Q_{latent} is the latent heat flux given by

$$Q_{\mathrm{latent}} = \rho_{\mathrm{air}} L_v C_d U_{10}(q_{\mathrm{sat}} - q), \qquad (3)$$

where $\rho_{\mathrm{air}} = 1.275$ kg m^{-3} is the air density, $L_v = 2.501 \times 10^6$ J kg^{-1} is the latent heat of evaporation, $C_d = 1 \times 10^{-3}$ is the drag coefficient (Frew et al. 2019) between the ocean and the atmosphere, U_{10} and q are the 10-m wind speed and the specific humidity we extract from ERA5, and q_{sat} is the saturation humidity calculated from

$$q_{\mathrm{sat}} = \frac{\epsilon_r e_w}{P_{\mathrm{atm}} - (0.378 e_w)}, \qquad (4)$$

with the ratio of molecular weight of water and dry air $\epsilon_r = 0.662$ and the saturated vapor partial pressure $e_w = 6.11e^{17.62\,\mathrm{SST}/(243.12+\mathrm{SST})} \times 10^2$. The Q_{sensible} is the sensible heat flux given by

$$Q_{\mathrm{sensible}} = \rho_{\mathrm{air}} C_{\mathrm{air}} C_d U_{10}(\mathrm{SST} - T_{2\mathrm{m}}), \qquad (5)$$

where $C_{\mathrm{air}} = 1005$ J kg^{-1} °C^{-1} is the heat capacity of air and $T_{2\mathrm{m}}$ is the 2-m air temperature from ERA5.

The reanalysis meteorological variables are area-averaged over four ERA5 grid points centered along 74°S, at 111.25°, 111.5°, 111.75°, and 112°W (white boxes in Fig. 1a), covering about 852 km^2 and most of the *EM959* observational site.

c. *Estimation of the accumulated sea ice formation from observations*

We make two thickness estimates of accumulated sea ice formation using the upper-ocean salt and heat budgets independently. Both the salt and heat budget estimations are made within the upper 150 m. We chose this depth as our observations below this depth do not show any significant trend in temperature or salinity, so are assumed to be below the atmospheric-influenced depth (see section 3 for details). A depth of 150 m also has the minimum variance in Conservative Temperature, Absolute Salinity, and potential density (Fig. S5), while still being always below the base of the mixed layer. *EM959* profiles used in both estimations are vertically averaged into 1-m bins. Single absent bins are filled by linear interpolation or extrapolation of the uppermost value to the surface; for reference, the uppermost value is always collected within the top 3 m. Profiles too shallow to reach 150 m are removed (in total 124 out of 513 profiles are omitted). This yields typically six profiles per day.

1) SEA ICE FORMATION CALCULATED FROM SALT BUDGET

Here, we assume that brine rejection caused by sea ice formation is the only significant process affecting the upper 150-m salt content, neglecting evaporation, precipitation, lateral advection, and vertical mixing/exchange between the top 150 m and deeper layers (see section 3 for details). Following Charrassin et al. (2008), the salt budget is described as

$$\rho_{\mathrm{old}} V_{\mathrm{old}} S_{\mathrm{A}_{\mathrm{old}}} = \rho_{\mathrm{new}} V_{\mathrm{new}} S_{\mathrm{A}_{\mathrm{new}}} + \rho_{\mathrm{ice}} V_{\mathrm{ice}} S_{\mathrm{A}_{\mathrm{ice}}}, \tag{6}$$

where ρ is the in situ density, V is the volume, and S_{A} is the Absolute Salinity at each depth level, with the subscript "old" for the original water properties, "new" for the water properties at a subsequent time, and "ice" for sea ice properties. Sea ice properties are assumed constant and chosen to be $S_{\mathrm{A}_{\mathrm{ice}}} = 7\,\mathrm{g\,kg}^{-1}$ (Biddle et al. 2017) and $\rho_{\mathrm{ice}} = 920\,\mathrm{kg\,m}^{-3}$ (Martin and Kauffman 1981; Biddle et al. 2017; Wilson et al. 2019). We further test different $S_{\mathrm{A}_{\mathrm{ice}}}$ and ρ_{ice} by recalculating the sea ice formation rate derived from the salt budget with varying values (Fig. S6) and confirm that the choice of those values does not affect our results qualitatively. The uncertainties caused by $S_{\mathrm{A}_{\mathrm{ice}}}$ and ρ_{ice} are negligible compared with the temporal variability. Given that this calculation is performed over a fixed depth range, the total volume does not change, so $V_{\mathrm{new}} = V_{\mathrm{old}} - V_{\mathrm{ice}}$. Substituting this into Eq. (6), we obtain the accumulated sea ice formation

$$V_{\mathrm{ice}} = \frac{V_{\mathrm{old}}(S_{\mathrm{A}_t}\rho_{\mathrm{new}} - \mathrm{S}_{\mathrm{A}_{\mathrm{old}}}\rho_{\mathrm{old}})}{S_{\mathrm{A}_{\mathrm{new}}}\rho_{\mathrm{new}} - S_{\mathrm{A}_{\mathrm{ice}}}\rho_{\mathrm{ice}}}. \tag{7}$$

.

The integral of V_{ice} over the upper 150 m gives the upper 150-m sea ice formation. The accumulated sea ice formation is then derived, using the cumulative sum of V_{ice} over the study period from yearday 52.

2) SEA ICE FORMATION CALCULATED FROM HEAT BUDGET

The heat content in the upper 150 m, $\mathrm{OHC}_{150\mathrm{m}}$, is calculated as

$$\mathrm{OHC}_{150\mathrm{m}} = \int_{z=-150\mathrm{m}}^{z=0\mathrm{m}} C_p \rho_z (\Theta_z - \Theta_{\mathrm{freezing}})\,dz, \tag{8}$$

where $C_p = 4000\ \mathrm{J\,kg}^{-1}\,{}^{\circ}\mathrm{C}^{-1}$ is the heat capacity of seawater, ρ_z and Θ_z are the in situ water density and Conservative Temperature of the water at the depth z, and $\Theta_{\mathrm{freezing}}$ is the in situ freezing point calculated using the TEOS-10 toolbox (McDougall and Barker 2011).

We assume that all heat loss from the ocean to the atmosphere is either used to cool the upper ocean or used to form sea ice. As with the salt budget, we neglect lateral advection and vertical exchange with water below 150 m. The relationship between the rate of change of $\mathrm{OHC}_{150\mathrm{m}}$, hereafter $d\mathrm{OHC}_{150\mathrm{m}}/dt$, and the heat flux used in sea ice formation $Q_{\mathrm{IceFormation}}$ is therefore

$$Q_{\mathrm{IceFormation}} = Q_{\mathrm{net}} - \frac{d\mathrm{OHC}_{150\mathrm{m}}}{dt}. \tag{9}$$

Hence, we calculate the time series of $Q_{\mathrm{IceFormation}}$, which is used to calculate the rate of change of sea ice volume using the following equation:

$$\frac{dV_{\mathrm{ice}}}{dt} = \frac{Q_{\mathrm{IceFormation}}}{L_f \rho_{\mathrm{ice}}}, \tag{10}$$

where $L_f = 3.35 \times 10^5\ \mathrm{J\,kg}^{-1}$ is the latent heat of fusion.

The accumulated sea ice formation is then derived as the time integral of dV_{ice}/dt over hourly intervals from yearday 52, as for the salt-budget-derived calculation.

d. *One-dimensional mixed layer model*

1) MODEL DESCRIPTION

We use a modified version of the Price–Weller–Pinkel (PWP) mixed layer model (Price et al. 1986). This model uses bulk formulas to incorporate the air–sea heat and salt fluxes. It has been further adapted by Lazarevich et al. (2004) to include vertical diffusion and subsequently developed by Biddle et al. (2017) to include a sea ice module and a turbulent kinetic energy parameterization. The mixing scheme now includes diffusion equations and three stability criteria: static stability, mixed layer (ML) stability (bulk Richardson number < 0.65), and shear flow stability (gradient Richardson number < 0.25). When the mixed layer depth changes, all ocean properties, including temperature, salinity, and horizontal water speeds, are averaged over the mixed layer.

To provide the initial hydrographic conditions for the model, we averaged the first 3 days of *EM959* temperature and salinity measurements into 2-m bins and then time averaged (Fig. 3). For consistency with the model, the initial

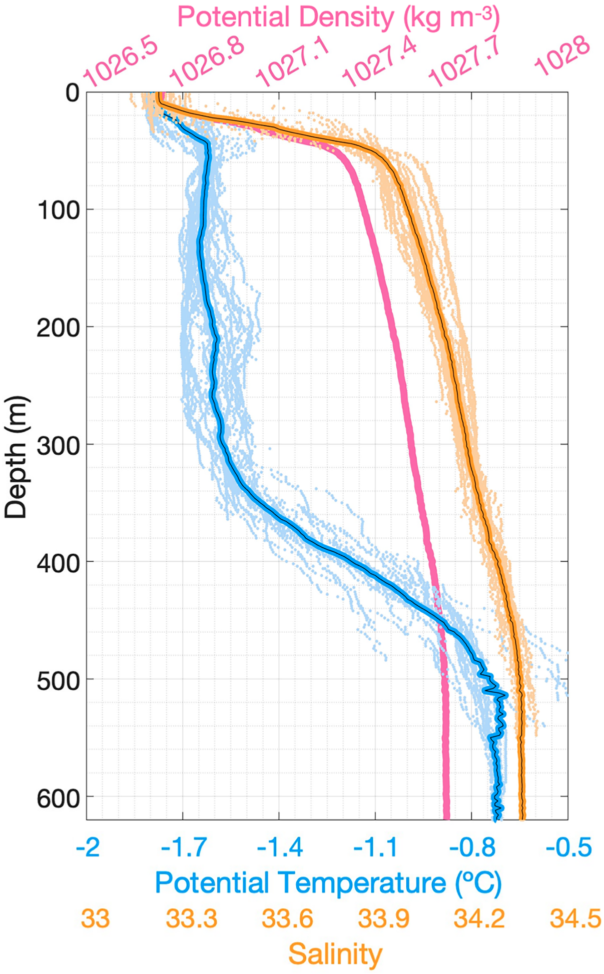

FIG. 3. The potential temperature (blue), practical salinity (orange), and potential density (pink) profiles used to initialize the model. Thick blue and orange lines indicate the first 3-day average of the *EM959* potential temperature and salinity measurements. Dots indicate the *EM959* measurements used to obtain the average profiles. The potential density profile (pink thick line) is calculated from the 3-day averaged salinity and temperature profiles.

hydrographic profiles use EOS-80 (Fofonoff 1983; i.e., potential temperature and practical salinity), but model outputs are converted to TEOS-10 (i.e., Conservative Temperature and Absolute Salinity; McDougall and Barker 2011) for plotting and comparison with observations. The initial horizontal velocity is zero for all model depths.

ERA5 hourly reanalysis data are linearly interpolated into 1-min resolution to generate atmospheric forcing fields for PWP. Biddle (2016) identifies the seawater optical properties in the southeastern Amundsen Sea as best described by Jerlov (1968) type 1A water, and we adopt this classification for solar radiation absorption. The seawater albedo used in the model is 0.06, consistent with Frew et al. (2019).

As described by Biddle et al. (2017), the model forms sea ice when the mixed layer has a temperature lower than the surface freezing point. The heat required to warm the mixed layer back to the freezing point is converted to sea ice formation using the latent heat of freezing. When the mixed layer gains heat from the atmosphere, this heat gain will initially melt the modeled sea ice, before it heats the ocean. If an excess of heat persists, it will then increase the mixed layer temperature. The model outputs an accumulated sea ice formation. The heat-budget-related parameters used in this model are consistent with those used for calculations from the observations [sections 2b and 2c(2)].

The model has 615 vertical layers of 1-m thickness. We run all simulations with a 1-min time step for 54 model days, covering the *EM959* measuring period. The model outputs are stored in 3-h intervals. The control simulation forced by ERA5 hourly reanalysis fluxes is named *ControlFlux* (Table 1; the control simulation and experiment names below are italicized to aid the reader).

2) MODIFICATION OF AIR–SEA HEAT FLUX IN THE MODEL

We introduce model forcings that have the air–sea heat flux (latent, sensible, shortwave, and longwave heat fluxes) adjusted to a certain percentage of their original values. These experiments are named *NoFlux*, *25%Flux* … , *150%Flux* (see Table 1 for details).

3) MODIFICATION OF MOMENTUM FLUX IN THE MODEL

To investigate the effect of momentum flux, we run a set of model experiments with momentum flux set to zero. They are named *ControlFlux+NoMomentum* and *NoFlux+NoMomentum* (see Table 1 for details). The wind speed (as used in the calculation of heat fluxes) remains the same as *ControlFlux*.

4) RELAXATION OF WATER COLUMN

To idealistically simulate the effect of lateral advection, we introduce relaxation of the water column into our *ControlFlux* simulation, referred to as *ControlFlux+Advection.* In these experiments, the entire water column temperature and salinity are relaxed to the initial profiles (i.e., observed measurements in mid-February) using the following equations:

$$T_{n_{\text{relaxed}}} = T_n + \text{RelaxationRate} \times (T_n - T_{\text{initial}}),$$

$$S_{n_{\text{relaxed}}} = S_n + \text{RelaxationRate} \times (S_n - S_{\text{initial}}),$$

where T_n and S_n are the modeled temperature and salinity profiles at time step n, T_{initial} and S_{initial} are the initial profiles, $T_{n_{\text{relaxed}}}$ and $S_{n_{\text{relaxed}}}$ are the relaxed modeled profile at time step n, and RelaxationRate is the relaxation rate for temperature and salt, respectively.

We test a range of relaxation rates varying from on the order of -10^{-7} to -10^{-4} (Fig. S7) and by visual inspection, find that the RelaxationRate $= 2 \times 10^{-5}$ provides results that fit the observed trends most closely.

e. Definition of the mixed layer depth, for observations and model results

We define the observed mixed layer depth (MLD) as the depth of maximum buoyancy frequency (i.e., stratification)

TABLE 1. Model experiment design. Simulation setups that are different from those used in the control simulation (*ControlFlux*) are highlighted in bold.

Experiment name	Heat flux	Momentum flux	Advection
NoFlux	**No** heat flux	Original momentum flux	No advection
25%Flux	**25%** of original heat flux	Original momentum flux	No advection
50%Flux	**50%** of original heat flux	Original momentum flux	No advection
75%Flux	**75%** of original heat flux	Original momentum flux	No advection
ControlFlux	Original heat flux	Original momentum flux	No advection
125%Flux	**125%** of original heat flux	Original momentum flux	No advection
150%Flux	**150%** of original heat flux	Original momentum flux	No advection
ControlFlux+NoMomentum	Original heat flux	**No** momentum flux	No advection
NoFlux+NoMomentum	**No** heat flux	**No** momentum flux	No advection
ControlFlux+Advection	Original heat flux	Original momentum flux	**With advection**

calculated on a 3-m vertically gridded and unsmoothed dataset. This identifies the sharpest pycnocline in each profile, consistent with the MLD defined by our bulk formula model. On average, this method detects an MLD that is 10.5 m deeper than the MLD calculated using a typical 0.03 kg m^{-3} density difference from the surface density (Fig. S8); and it is less likely to be affected by small-scale density perturbations occurring at the sea surface, that might be caused by sea ice formation or melting. The identification methods of the MLD do not affect our results qualitatively. For reference, the resultant MLD is not sensitive to the choice of bin size, but a 3-m bin size effectively eliminates the effect of small-scale noise. Outliers in the calculated MLD are removed following visual inspection.

The modeled MLD is defined at each time step in the model run. The model will mix the water column downward from the sea surface until the water column is gravitationally stable and the vertical shear of horizontal velocity is not sufficient to break the stratification. The critical gradient Richardson number and the critical bulk Richardson number are set to 0.25 and 0.65, respectively. The Richardson numbers were determined in laboratory experiments (Miles 1961; Howard 1961) and have been used in the sea ice–covered Southern Ocean (Wilson et al. 2019) and the Amundsen Sea (Biddle et al. 2017).

3. Observed intense cooling, salinification, and mixed layer deepening

During February–April (*EM959*) and from May to September (MEOP), the mixed layer temperature is always close to the freezing point (i.e., <-1.6°C), while salinity and density generally increase over time from about 33.3 g kg^{-1} and 1027 kg m^{-3} (around yearday 52) to 34.1 g kg^{-1} and 1027.4 kg m^{-3} (around yearday 106), due to sea ice formation and brine rejection (Figs. 4 and 5b). As a result, the upper-ocean water experiences vertical convection that contributes to the deepening of the mixed layer over time, from about 25 to 125 m (white lines with black edges in Fig. 5). At the start of our observations in mid-February, the surface water is already close to the freezing point, but the salinity is relatively fresh (around 33.4 g kg^{-1}); it becomes gradually more saline due to sea ice formation as the surface water transitions from Antarctic Surface Water to Winter Water (Fig. 4). Below around 150 m, the hydrographic properties do not show any clear temporal variation during our study period (Fig. 4b). This seasonal stratification erodes gradually in autumn, as evidenced by the reducing stratification at and immediately below the base of the mixed layer (i.e., the red line indicating strong stratification in Fig. 5c becomes less visible). The MEOP seal-tag observations show that the mixed layer salinification continues through May (blue circles in Fig. 4b). By September (dark gray dots and lines in Fig. 4b), the upper 400-m water column is uniformly cold and dense, although warm mCDW persists at depth throughout the observations.

The observed upper 150-m heat content generally decreases during the study period (Fig. 6a), caused by the negative net heat flux (i.e., ocean losing heat) on most EM959 days (Fig. 2a). Compared to the nearly monotonic increases in salt content, the decreases in heat content are slower and more variable because the mixed layer temperature has been near the freezing point, meaning the heat loss from the ocean to the atmosphere is compensated largely by the intense sea ice formation. This is evident from the increased salinity, aligning with brine rejection during this period of sea ice formation (Fig. 6b). Streak patterns in sea ice imagery (Fig. 1 and Fig. S9) are also consistent with previous observations of frazil ice being blown offshore by the winds (Wadhams et al. 2018) indicating sea ice formation.

Significant changes in the top 150-m heat content require a further deepened mixed layer, which has not occurred in the observations, likely due to advective heat, which will be discussed in section 5. The time-average net air–sea heat flux is -134.5 W m^{-2} (i.e., ocean losing heat) over the 53 days of the study period (Fig. 2a), equivalent to the latent heat required to form 3.8 cm per day of sea ice [Eq. (10)], or cool the upper 150-m column by 0.018°C per day [Eq. (8)].

The net air–sea freshwater flux (i.e., precipitation minus evaporation, Fig. 2c) is 1.11×10^{-8} m s^{-1}, equivalent to 0.1 cm per day of sea ice melt; this figure is negligible compared with the heat-derived and salt-derived sea ice formation rates of about 3 cm per day (Fig. 6c), so hereafter, we neglect air–sea freshwater flux in the following model simulations in section 4.

The trends in the two independently derived sea ice formation rates (from the heat and salt budgets) agree strikingly well ($R = 0.92$; black and gray lines, respectively, in Fig. 6c).

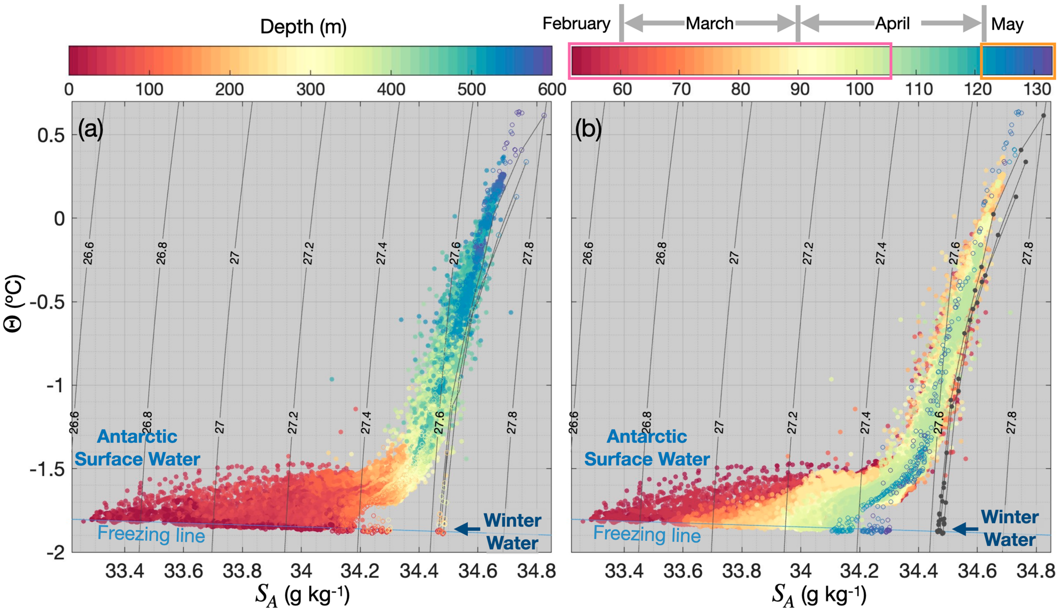

FIG. 4. Conservative Temperature–Absolute Salinity (Θ–S_A) diagrams, colored by (a) depth and (b) yearday of measurement, with potential density contours overlaid in black. Filled dots show the recovered *EM959*, with yearday range indicated by the pink rectangle in the color bar above (b). Open circles show MEOP measurements from 1 to 13 May 2014, with yearday range indicated by the orange rectangle. Circles connected by gray lines are measurements from 1 Sep 2014; they are colored in dark gray in (b). Observations obtained on later dates overlie observations obtained on earlier dates.

To avoid including the influence of short-term events on the calculated sea ice formation rate, we use linear regression to obtain representative sea ice formation rates over the study period. The sea ice formation rates are estimated to be 3.6 cm per day from the heat budget and 2.8 cm per day from the salt budget, using the “robust fit” method (i.e., an iteratively reweighted least squares algorithm; Holland and Welsch 1997). For reference, before yearday 95 (when the rates begin to diverge), the sea ice formation rates are estimated to be 3.1 cm per day from the heat budget and 2.9 cm per day from the salt budget. Given that our calculations for sea ice formation rates are determined from the temporal changes in salinity and temperature, it is unlikely that any potential systematic *EM959*-related bias in the salinity measurements would impact our results.

The sea ice formation rates derived from our upper-ocean heat/salt budget analysis (3.6 and 2.8 cm per day) are slightly lower than our previous estimation relying solely on the net heat flux (3.8 cm per day). There are several possible explanations for this discrepancy. First, much of the mixed layer is not at the freezing point at the beginning of the study period, so additional heat loss is required to cool the mixed layer, instead of forming sea ice. Second, a portion of the net heat flux change is offset by heat transported from the subsurface to the near-surface layers, subsequently impacting the calculated sea ice formation rate. We observed several short-term increases in heat content in the layer between 150 and 250 m during yeardays 95–103 (Fig. 5; Fig. S10), when the net heat loss from the ocean to the atmosphere is intense (Fig. 2), indicating that heat from below 150 m enters the top-150 m. This upward flux of heat through the ocean will contribute to slowing the formation rate of the sea ice. Ackley et al. (2015) reported an ocean-to-fast-ice heat flux near Bear Island from February to March 2009 of approximately 17 W m^{-2}, equivalent to a sea ice melt of about 0.4 cm per day, which is comparable to our calculated discrepancy mentioned earlier. Additional discrepancies between the heat- and salt-budget-derived sea ice formation rates could partly be caused by fluctuations in glacial meltwater inputs. Assuming an initial salinity of 34 g kg^{-1}, if meltwater inputs increased by a 0.1%, this would reduce the overall salinity by approximately 0.034 g kg^{-1}, causing a decrease in the salt-budget-derived sea ice formation by about 0.13 cm. Moreover, due to the lack of observations upstream of our study region, we cannot provide a reliable estimate of the effect of lateral advection on the upper-ocean properties. Hence, the lateral advection, that might transport heat and freshwater into and out of our study region, is not included in the sea ice formation rate calculation.

4. Modeled one-dimensional upper-ocean processes

To better understand the main controls on the observed upper-ocean evolution, we run a one-dimensional model (PWP, described in section 2d) and isolate different processes in different model experiments (Table 1). We first hypothesize that the air–sea heat flux determines the upper-ocean evolution, neglecting freshwater flux (see section 3 for details), momentum flux (discussed later in section 4c), and horizontal advection

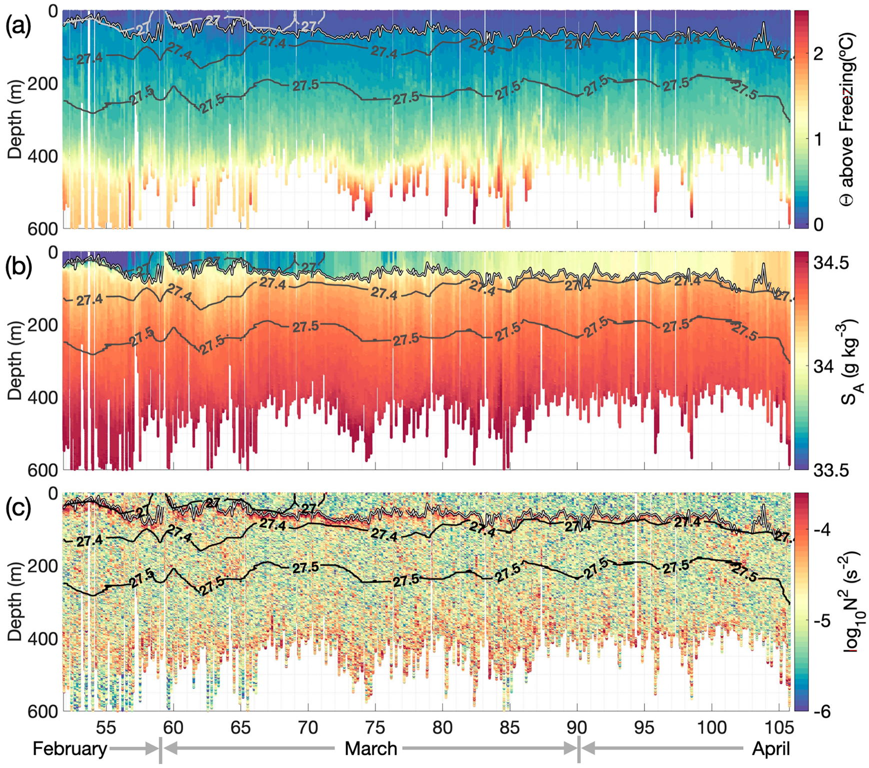

FIG. 5. Time series of (a) Conservative Temperature (Θ) above freezing, (b) Absolute Salinity (S_A), and (c) stratification ($\log_{10}N^2$) from observations collected by EM959 in our study region (pink circle and pink rectangle in Fig. 1a). Thick gray/black lines denote the potential density. Thin white lines with black edges denote MLD.

(discussed later in section 5). We evaluate the control run of this model in section 4a and then run two sets of conceptual experiments in sections 4b and 4c.

a. *Evaluation of modeled upper-ocean processes*

Similar to the *EM959* observations, the *ControlFlux* simulation exhibits decreasing heat content, increasing salt content, accumulated sea ice formation, and a deepening mixed layer over the study period (light green lines in Fig. 6) showing generally monotonic trends. Although the *ControlFlux* does not capture the observed short-term fluctuations (black and gray lines in Fig. 6), sea ice formation and salt content from the *ControlFlux* are similar to the observations. However, the *ControlFlux's* heat content decreases significantly more rapidly, and the mixed layer deepens faster (light green lines in Fig. 6). On the final model day, *ControlFlux's* upper 150-m heat content is approximately half of the observed value, and *ControlFlux's* MLD is about double the observed value.

The southern Amundsen Sea is a complex location for the ERA5 reanalysis, and the selected grid points are located at the edge of the boundary between the ice shelf, land, and ocean. Our four ERA5 grid points chosen for model forcing are marked as being 1.5%–2% covered by land, potentially leading to erroneous near-surface conditions. However, additional experiments with surface forcing derived from ERA5 grid points further north of our original grid points suggest that the systematic difference between the observations and the *ControlFlux* does not appear to be caused by the ERA5 ice/land/open-ocean mask.

Based on satellite observations (using corrected reflectance from MODIS *Terra* true color product, Worldview; Fig. S9), intermittent thin sea ice covered the study region. Thin sea ice will dampen air–sea fluxes (Maykut 1978) and change the drag coefficient (Lüpkes and Birnbaum 2005), thus modifying both air–sea heat and momentum fluxes (Auger et al. 2022), yet thin sea ice is not well constrained in ERA5 due to limited observations. Additionally, air–sea fluxes derived from the ERA5 reanalysis could potentially have biases, such as colder air temperature and underestimated high wind speeds (Jones et al. 2016). We therefore suspect that the fluxes we use to force the model may differ from the actual fluxes experienced by the ocean, leading to discrepancies between the model results and the observations. We also acknowledge that there are uncertainties in the fluxes due to other short-term processes like passing storms or other short-lived meteorological events. However, due to the complex nature of the air–ice–ocean system and the limited sea ice and near-surface ocean observations, it is impossible to obtain precise uncertainties in the fluxes. Therefore, we designed our idealized model experiments to explore a full range of scenarios that are known to occur in reality. Our intention is not to reproduce the exact air–ice–ocean interactions but to mimic the potential effects

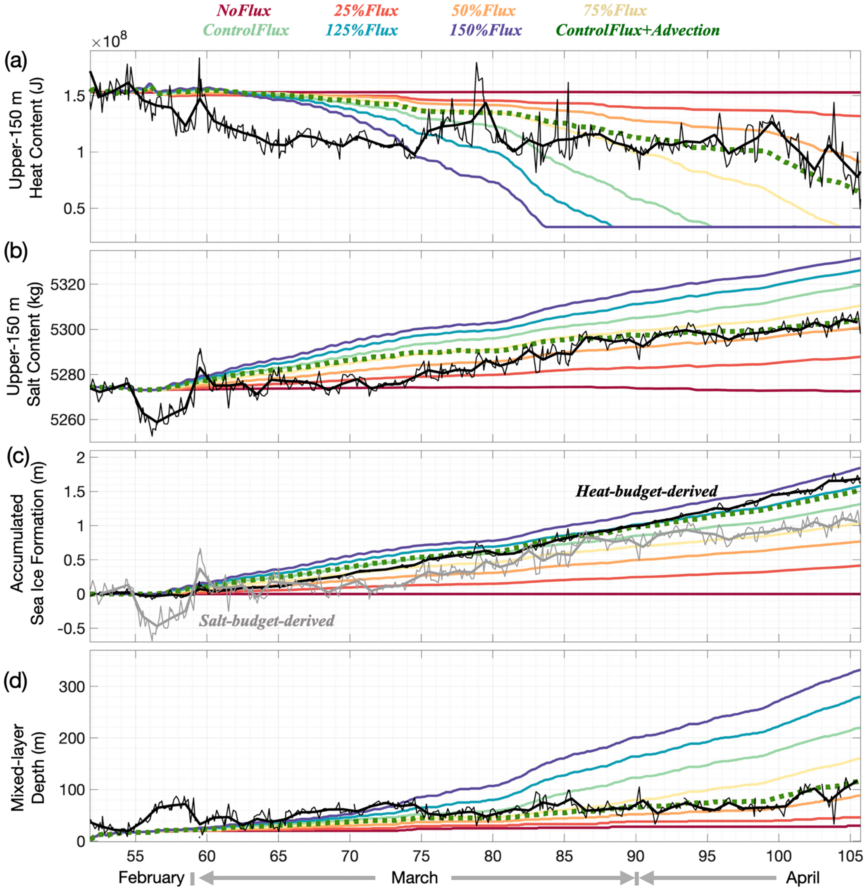

FIG. 6. Comparison of upper-ocean quantities derived from *EM959* observations (thin black lines, with thick lines for daily mean) and models forced with different heat flux (colored lines, with thick dotted dark green line for *ControlFlux+Advection* run). (a) Upper 150-m heat content. (b) Upper 150-m salt content. (c) Accumulated sea ice formation, with black for heat-budget-derived ice formation and gray for salt-budget-derived ice formation. (d) MLD.

that these different scenarios might have on the air–sea heat and momentum fluxes. Therefore, different simulations forced by reduced or increased heat fluxes or with or without momentum fluxes are explored to assess the upper-ocean response under these different forcings.

b. *The modeled upper-ocean processes forced with different heat flux*

All of our model experiments (Table 1) reproduce mixed layers that experience gradual cooling, salinification, and deepening over time, but at different rates depending on the magnitude of the heat fluxes (Fig. 6). Reduced air–sea heat flux from ocean to atmosphere results in slower upper-ocean cooling, salinification, and mixed layer deepening (Fig. 7), and vice versa when the air–sea heat flux is increased. Consequently, the mixed layer salinification and deepening are the strongest in *150%Flux* and the weakest in *NoFlux* (Fig. 7), as expected.

The observed trends in upper 150-m ocean heat and salt contents are most similar to the *50%Flux simulation* (Fig. 6), indicating that the reduced heat flux does improve the model results and achieve a better prediction than the *ControlFlux*. However, the sea ice formation and MLD are significantly different, indicating that the reduction in heat flux is not sufficient to explain the upper-ocean evolution. We therefore explore whether momentum flux or lateral advection plays a role in determining the upper-ocean evolution.

c. *Effect of momentum flux*

The presence of sea ice might increase or decrease the momentum flux between the ocean and the atmosphere (Meneghello et al. 2018). To estimate the impact of momentum flux on the upper-ocean processes, we run two additional sensitivity tests with the momentum fluxes switched on and off.

When there is no heat flux, the momentum flux increases the MLD considerably (about 20 m; orange and blue lines in Fig. 8). However, with heat fluxes as specified in the *ControlFlux*, the maximum difference between the modeled MLD with and without momentum is 3 m (overlapping red and green lines in Fig. 8), negligible compared with a ~150-m deep mixed layer.

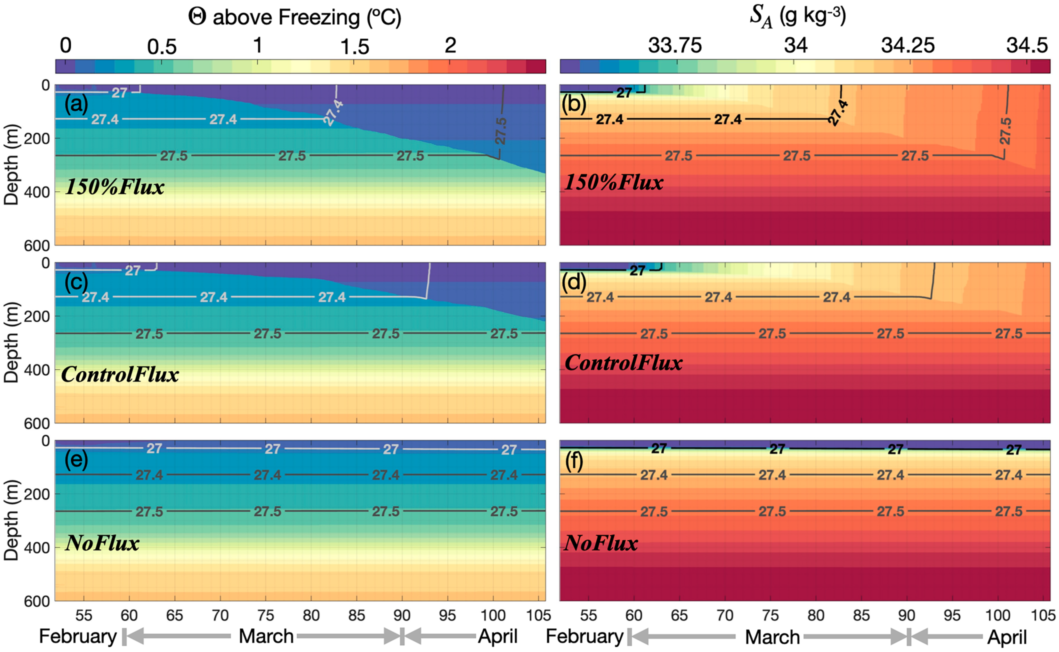

FIG. 7. Examples of time series of the modeled temperature and salinity. (a),(b) *150%Flux*, (c),(d) *ControlFlux*, and (e),(f) *NoFlux*. Contours indicate the potential density. The color schemes are the same as in Fig. 5.

The explanation for the small influence of momentum fluxes on upper-ocean processes is due to the substantial depth of the mixed layer during the study period (typically deeper than 50 m). The modeled mixed layer gains momentum from wind stress, which is distributed uniformly throughout the layer. Consequently, the horizontal water speed remains constant within the mixed layer and drops to nearly zero below it. Therefore, given the same wind forcing, and consequently the same momentum flux, a deeper mixed layer results in a lower horizontal water speed within the layer, leading to reduced vertical shear at its base. The substantial depth of the mixed layer during the study period results in a very weak vertical shear, typically less than 0.05 m s^{-1} difference across the base of the mixed layer (Fig. S11). This weak shear, compared with the high stratification at the base of the mixed layer, leads to high gradient and bulk Richardson numbers that are not sufficiently low to trigger mixing at the base of the mixed layer in the model. We expect similar processes to occur in reality, where the wind stress stirs the mixed layer, but fails to effectively penetrate a deep mixed layer. This implies that buoyancy forcing dominates over wind forcing in driving vertical processes in the water column in this regime, especially in autumn when heat loss is intense, leading to the creation of a deep mixed layer.

5. The role of advection

a. *Effect of advection on the upper-ocean processes*

In this section, we evaluate the potential role of the advection of water with different properties in influencing the observed heat budget and sea ice formation rates at the study site. Previous research, using observations and/or models, has documented the presence of coastal currents, flowing west

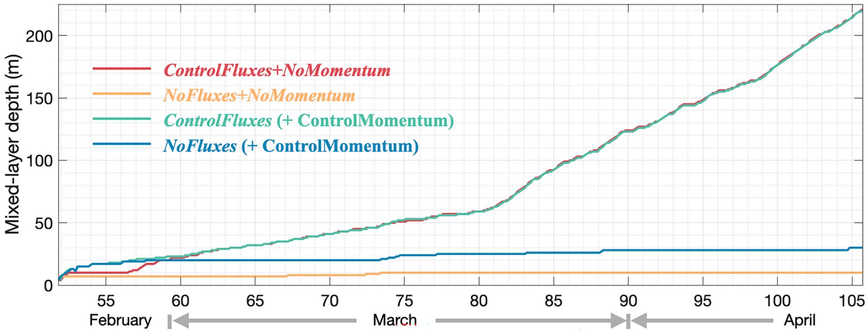

FIG. 8. The comparison among simulations with altered momentum flux and/or heat and freshwater fluxes. The green line overlies the red line.

from the southeastern Amundsen Sea along the coast (Biddle et al. 2017; St-Laurent et al. 2017). The coastal current and eddies carried with it may transport water from east of Bear Ridge (Fig. 1) to our study site [as shown by the modeling study of St-Laurent et al. (2017)]. The sea ice east of Bear Ridge consists of mainly fast ice, which is distinctly thicker and more uniform than the observed frazil-ice-dominated conditions in the ASP (Fig. 1). Thicker ice can reduce ocean heat loss by more than one order of magnitude compared to air–sea fluxes over open-ocean or even over thin sea ice–covered areas [e.g., ocean heat loss was ~17 W m^{-2} beneath fast ice east of the ASP as reported by Ackley et al. (2015), compared to ~135 W m^{-2} as estimated over the ASP, see section 3 for details; Maykut 1978]. This suggests that ocean conditions beneath the fast ice-covered region would be significantly different from those observed in our study region.

Given these differences in oceanic conditions and the presence of coastal currents, we hypothesize that water advected into our study area from beneath the fast ice has been insulated from the effects of high sea ice formation for some time, and is thus likely to be fresher, and maybe even warmer than the water in our study region. We assume that this water mass will have been exposed to the atmosphere during the early summer and thus expect the salinity under the Bear Ridge fast ice to be close to that of Antarctic Surface Water, while the temperature is likely to be close to the surface freezing point.

Additionally, the salt-budget-derived sea ice formation rate is lower than the heat-budget-derived sea ice formation rate, especially in April (Fig. 6c). This discrepancy may be due to the influence of the coastal current or input of glacial meltwater, which can bring extra heat and/or freshwater into our study area. Such input can increase the heat content and reduce the salt content, resulting in a higher sea ice formation rate when using the heat budget and a lower rate when using the salt budget. This further motivates our experiments adding a relaxation term mimicking the effect of advection by the coastal current.

b. *Idealized experiment to reproduce the effect of advection*

To reproduce the potential effect of coastal currents, we designed another set of experiments, *ControlFlux+Advection*. Here, we assume that, over the period of our study, water east of Bear Ridge would be insulated from surface fluxes and experience minimal salt input from sea ice formation, thus preserving water properties similar to late summer (i.e., approximating water properties similar to yearday 52). To test the possible influence of this advection, we relax the water masses to the initial profile with a range of time scales to represent varying rates of advection (see section 2).

From the range of tested relaxation rates, we find that 2×10^{-5} gives the closest match to the observed trends in heat and salt budgets, sea ice formation rates, and mixed layer depth (Fig. S7), assuming that the control fluxes are accurate. On average, a relaxation rate of 2×10^{-5} in our mixed layer increases the temperature by 3.5×10^{-3}°C and decreases the salinity by 7.5×10^{-3} per day (Fig. S12). Assuming a typical water speed of 15 cm s^{-1} in the Amundsen Sea coastal current, this would require a horizontal temperature gradient of 2.7×10^{-4}°C km^{-1} and a salinity gradient of 5.8×10^{-4} g kg^{-1} km^{-1}, which is not unrealistic, based on typical Amundsen Sea hydrography. We acknowledge that we do not have observations upstream to validate whether our relaxation matches the effect of local advection, nor can we be sure that a different combination of heat fluxes and advection might not provide as good a match. Nevertheless, our results demonstrate that advection is required to match the observed trends. Our aim is not to obtain a realistic advection rate, but to demonstrate that advection is an important driver of upper-ocean processes.

Compared with the *ControlFlux* simulation, the *ControlFlux+Advection* simulation shows a slower rate of upper-ocean heat/salt content reduction and mixed layer deepening. This indicates that the advection of fresher and warmer water in the mixed layer slows down upper-ocean heat-content reduction (Fig. 6a, dark green line) and stabilizes the MLD (Fig. 6d, dark green line). With a shallower MLD, less heat is entrained into the mixed layer from the deeper ocean to compensate for the heat loss to the atmosphere. Since the mixed layer is already at the freezing point, extra heat loss will then be used to form sea ice; this results in an increase in sea ice formation (Fig. 6b, dark green line). The *ControlFlux+Advection* simulation reproduces trends very similar to the observations. In the final model formulation, the *ControlFlux+Advection* simulation presents a sea ice formation rate of 2.9 cm per day, an MLD of 117 m, and top-150-m heat and salt contents of 2.31×10^8 J and 8829 kg, respectively; for reference, the sea ice formation rate estimated from observations is 2.8 cm (salt-budget derived) or 3.8 per day (heat-budget derived), the last-day-averaged MLD of 117 m, and top 150-m heat and salt contents of 2.21×10^8 J and 8830 kg, respectively.

We acknowledge that advection of different water properties or varying stratification beneath the mixed layer can lead to distinct mixed layer responses. If the advected water is warmer and less fresh than in our simulation, it may not provide enough buoyancy to sufficiently slow the mixed layer deepening, potentially failing to counterbalance the heat carried by the advection, which could reduce sea ice formation. Similarly, if the stratification beneath the mixed layer is weaker than in our simulation, the mixed layer might deepen more readily so that a stronger buoyancy injection is required to stabilize the mixed layer deepening. A detailed three-dimensional model, driven by accurate boundary conditions and forcing, would undoubtedly provide additional insights. However, the simple relaxation experiment described above allowed us to explore the degree to which a one-dimensional model can simulate the observed upper-ocean evolution and to discuss the relative importance of advection. Our model results also suggest that any estimate of sea ice formation rate derived using only ERA5 air–sea fluxes and ocean observations, without including a three-dimensional ocean component, is likely to be underestimated. This caveat also applies to the sea ice formation rates derived from our heat and salt budget in section 3. This is because such estimations do not account for the additional heat and freshwater contributions from horizontal advection processes. Consequently, the calculated sea ice formation rate is the minimum possible rate, with the actual rate potentially being higher due to these unconsidered factors. Unless colder, saltier water was advected into our study region, which is unlikely, based on historical measurements of coastal currents in this area.

6. Further discussion

The PWP model effectively reproduces the trends in the observed heat content, accumulated sea ice formation, and mixed layer deepening when appropriate atmospheric forcing and simulated advection are applied. Our results indicate that both one-dimensional processes, such as air–sea interactions and entrainment from below the mixed layer, as well as advection, play crucial roles in the upper-ocean evolution. Specifically, in our study area, the deep mixed layer means that wind stirring is less effective at penetrating the base of the mixed layer and influencing the water below it. Consequently, buoyancy flux dominates over momentum flux. Our idealized experiments mimicking advection suggest that when horizontal advection introduces heat and freshwater to the mixed layer, it reduces mixed layer deepening and thus increases the sea ice formation rate. These findings imply that sea ice formation is influenced by a range of factors that cannot be accurately captured by considering air–sea interactions alone.

In addition to the overall seasonal evolution, the observations also show short-term variability, such as rapid cooling and salinification (Figs. 5 and 6). We identify several processes that may contribute to short-term variability. First, high wind events such as katabatic winds can result in short-term cooling events that are not captured by ERA5 (Jones et al. 2016), and thus also missed in the model results. Second, vertical mCDW intrusion might have occurred during the observing period. The intrusion of warm mCDW from deeper layers has been measured, by an ice mass balance buoy deployed to the east of Bear Island on pack ice, and was reported to affect sea ice thickness (Ackley et al. 2015). Similarly, in the West Antarctic Peninsula, vertical intrusions of mCDW at daily time scales were observed by moorings and estimated to affect sea ice growth (Saenz et al. 2023), indicating this might be a common feature of warm shelf seas. However, those processes involving vertical water intrusions are unlikely to be surface-driven and so can only be validated by hydrographic measurements. Third, rapid vertical fluctuations of the isopycnals could be caused by passing eddies, internal waves, or topographic Rossby waves (Wåhlin et al. 2016; St-Laurent et al. 2017). For instance, after day 100, there is a rapid deepening of the deep isopycnals concurrent with the mixed layer deepening, likely due to wave activity or advective fluxes. This process drives the cooling of the top 150 m, contributing to a noticeable shift in the trends. The sea ice–corrected satellite altimetry sea surface height anomaly dataset (Auger et al. 2022) did not reveal any detectable eddy features corresponding to the rapid upper-ocean changes we observed. We further conduct a spectrum analysis of EM959 temperature and salinity measurements, which do not reveal any dominant short-term frequencies. Finally, Ekman pumping near the ice edge could also contribute to the observed vertical movement of the pycnoclines (Xu et al. 2023). However, Ekman pumping in our study region calculated from ERA5 winds does not present a significant correlation with the abrupt mixed layer depth changes (Fig. S13) so its contribution appears to be limited.

Satellite-based sea ice formation calculations typically focus on air–sea heat fluxes, largely ignoring ocean conditions due to limited observations. Our observations indicate that as the mixed layer deepens, ocean heat from below is entrained upward, compensating for the heat loss from the ocean to the atmosphere that could otherwise form sea ice. Consequently, the actual sea ice formation rate may be lower than satellite-based estimates. However, our model results, which include advection, suggest that when horizontal advection brings freshwater and/or heat to the upper ocean, it reduces mixed layer deepening and thus increases the sea ice formation rate. If mixed layer deepening is significantly dampened, nearly all ocean heat loss would contribute to sea ice formation. Therefore, the accuracy of satellite-based sea ice formation estimates depends on whether horizontal advection counteracts 1D processes, preventing or significantly slowing mixed layer deepening. Based on satellite microwave radar observations and reanalyses, Nihashi and Ohshima (2015) estimated an average sea ice formation rate of 3 cm per day (with a range of 2.3–3.8 cm per day; Fig. S14) in March and April between 2003 and 2010 within our study area (indicated by the pink circle in Fig. 1). This is comparable to our calculated sea ice formation rates, but only because, in this location, advection inhibits rapid mixed layer deepening, offsetting the potential overestimation by satellite-based methods.

In summer months, or in some of the Antarctic shelf seas where the water beneath the mixed layer is not primarily influenced by the relatively warm mCDW, the potential input of heat stored beneath the mixed layer is negligible compared with the solar radiation (e.g., Prydz Bay; Aoki et al. 2022). Hence, while the advection of the warmer and fresher water may slow down the mixed layer deepening, we do not anticipate a notably enhanced sea ice formation. This is because a shallower mixed layer does not transport sufficient heat to significantly impact the sea ice formation rate when solar radiation remains the dominant source of heat driving sea ice melt.

7. Conclusions

In this study, we use a full-depth high vertical-resolution hydrographic dataset measured by a recovered seal tag to investigate upper-ocean processes close to the Antarctic continent during austral autumn (from mid-February to late-April). Our observations reveal upper-ocean cooling, salinification and densification, and the consequent erosion of stratification. Our observations also capture a gradual mixed layer deepening with several abrupt deepening/cooling events (Figs. 5 and 6). An average sea ice formation rate of ~3 cm per day and a mixed layer deepening of ~2 m per day are estimated and are comparable to previous studies (Charrassin et al. 2008; Nihashi and Ohshima 2015). We use a 1D mixed layer model to investigate the possible mechanisms controlling the upper-ocean processes with a focus on exploring the influence of air–sea heat flux. Our simulations with reduced/enhanced air–sea heat flux demonstrate that the observed mixed layer deepening and salinification are most consistent with simulations where the heat flux is reduced by 50% relative to ERA5. However, the upper-ocean salt content and two independent sea ice budget calculations are most consistent with simulations forced by unmodified ERA5 heat fluxes. One possible explanation for this apparent discrepancy is the advection of water from under fast ice east of the ASP, which would increase near-surface stratification and impede mixed layer deepening. To test this potential influence, we run extra simulations. Our simulation with idealized advection agrees remarkably well with the ASP observations. This emphasizes the importance of three-dimensional processes, both within and beneath the mixed layer. Understanding the sea ice formation processes in polynyas previously limited by sparse observations is of high interest to ocean and cryosphere research.

Our study presents the first estimate of the sea ice formation rate in the southeastern Amundsen Sea during the rarely observed autumn months. The high productivity of the ASP has been attributed to upper-ocean processes that entrain nutrients into the euphotic zone. Our observations present the first insights into those upper-ocean processes during autumn. Moreover, the ASP is surrounded by some of the most rapidly melting ice shelves, and ocean processes in the ASP influence, and influenced by ocean–ice shelf interactions that drive basal ice shelf melt. Our results could therefore be used to validate the variability of the upper ocean in climate models and their representation of sea ice formation.

Acknowledgments. We thank the scientists, technicians, officers, and crew working on the Ocean2Ice (RRS *James Clark Ross* 2014, chief scientist: Karen J. Heywood) and ITGC (RV *Nathaniel B. Palmer* 2020, chief scientist: Julia S. Wellner) cruises for enabling data collection. We are grateful to Mike Fedak and Simon Moss who tagged the seals and Mark Barham, Lars Boehme, and Guilherme A. Bortolotto who found this tag EM959 and decoded it. This work was supported by projects Ocean2ice (NERC Grant NE/J005703/1; K. J. H., B. G. M. W., D. P. S.), TARSAN (NERC Grant NE/S006419/1; Y. Z., K. J. H, R. A. H.), ARTEMIS (NERC Grant NE/W007045/1; Y. Z., K. J. H., S. E. S., R. A. H.), and COMPASS (European Research Council Horizon 2020 advanced Grant 741120; K. J. H., Y. Z., R. A. H.). Yixi Zheng was partially supported by the China Scholarship Council and the University of East Anglia.

Data availability statement. Full-resolution EM959 measurements are openly available at https://doi.org/10.5281/zenodo.10478505. All model codes and plotting codes are stored at https://github.com/YixiZheng/MixedLayerModelCodes. MODIS Terra true colour corrected reflectance product images were obtained via Worldview, https://worldview.earthdata.nasa.gov/?v=-1837628,-754584,-1374835,-497744&r=97&p=antarctic&z=2&l=MODIS_Terra_L3_SST_Thermal_4km_Night_Daily(hidden),Coastlines_15m,MODIS_Terra_CorrectedReflectance_TrueColor&lg=false&t=2014-03-23-T00%3A19%3A15Z. Sea ice production data were obtained from http://www.lowtem.hokudai.ac.jp/wwwod/polar-seaflux/southern-ocean/AMSR-LATLON/.

REFERENCES

Ackley, S. F., H. Xie, and E. A. Tichenor, 2015: Ocean heat flux under Antarctic sea ice in the Bellingshausen and Amundsen Seas: Two case studies. *Ann. Glaciol.*, **56**, 200–210, https://doi.org/10.3189/2015AoG69A890.

Aoki, S., T. Takahashi, K. Yamazaki, D. Hirano, K. Ono, K. Kusahara, T. Tamura, and G. D. Williams, 2022: Warm surface waters increase Antarctic ice shelf melt and delay dense water formation. *Commun. Earth Environ.*, **3**, 142, https://doi.org/10.1038/s43247-022-00456-z.

Arrigo, K. R., K. E. Lowry, and G. L. van Dijken, 2012: Annual changes in sea ice and phytoplankton in polynyas of the Amundsen Sea, Antarctica. *Deep-Sea Res. II*, **71–76**, 5–15, https://doi.org/10.1016/j.dsr2.2012.03.006.

Auger, M., J.-B. Sallée, P. Prandi, and A. C. Naveira Garabato, 2022: Subpolar Southern Ocean seasonal variability of the geostrophic circulation from multi-mission satellite altimetry. *J. Geophys. Res. Oceans*, **127**, e2021JC018096, https://doi.org/10.1029/2021JC018096.

Bett, D. T., P. R. Holland, A. C. N. Garabato, A. Jenkins, P. Dutrieux, S. Kimura, and A. Fleming, 2020: The impact of the Amundsen Sea freshwater balance on ocean melting of the West Antarctic Ice Sheet. *J. Geophys. Res. Oceans*, **125**, e2020JC016305, https://doi.org/10.1029/2020JC016305.

Biddle, L. C., 2016: Identifying glacial meltwater in the Amundsen Sea. Ph.D. thesis, School of Environmental Sciences, The University of East Anglia, 185 pp., https://ueaeprints.uea.ac.uk/id/eprint/59385/1/2016BiddleLCPhD.pdf.

——, K. J. Heywood, J. Kaiser, and A. Jenkins, 2017: Glacial meltwater identification in the Amundsen Sea. *J. Phys. Oceanogr.*, **47**, 933–954, https://doi.org/10.1175/JPO-D-16-0221.1.

Boehme, L., P. Lovell, M. Biuw, F. Roquet, J. Nicholson, S. E. Thorpe, M. P. Meredith, and M. Fedak, 2009: Technical Note: Animal-borne CTD-Satellite Relay Data Loggers for real-time oceanographic data collection. *Ocean Sci.*, **5**, 685–695, https://doi.org/10.5194/os-5-685-2009.

Charrassin, J.-B., and Coauthors, 2008: Southern Ocean frontal structure and sea-ice formation rates revealed by elephant seals. *Proc. Natl. Acad. Sci. USA*, **105**, 11 634–11 639, https://doi.org/10.1073/pnas.0800790105.

Chelton, D. B., R. A. deSzoeke, M. G. Schlax, K. El Naggar, and N. Siwertz, 1998: Geographical variability of the first baroclinic Rossby radius of deformation. *J. Phys. Oceanogr.*, **28**, 433–460, https://doi.org/10.1175/1520-0485(1998)028<0433:GVOTFB>2.0.CO;2.

Elvidge, A. D., I. A. Renfrew, A. I. Weiss, I. M. Brooks, T. A. Lachlan-Cope, and J. C. King, 2016: Observations of surface momentum exchange over the marginal ice zone and recommendations for its parametrisation. *Atmos. Chem. Phys.*, **16**, 1545–1563, https://doi.org/10.5194/acp-16-1545-2016.

Fedak, M., 2004: Marine animals as platforms for oceanographic sampling: A "win/win" situation for biology and operational oceanography. *Mem. Natl. Inst. Polar Res.*, **58**, 133–147.

——, P. Lovell, B. McConnell, and C. Hunter, 2002: Overcoming the constraints of long range radio telemetry from animals: Getting more useful data from smaller packages. *Integr. Comp. Biol.*, **42**, 3–10, https://doi.org/10.1093/icb/42.1.3.

Fofonoff, N. P., and R. C. Millard Jr, 1983: Algorithms for the computation of fundamental properties of seawater. UNESCO, 53 pp., https://doi.org/10.25607/OBP-1450.

Frew, R. C., D. L. Feltham, P. R. Holland, and A. A. Petty, 2019: Sea ice–ocean feedbacks in the Antarctic shelf seas. *J. Phys. Oceanogr.*, **49**, 2423–2446, https://doi.org/10.1175/JPO-D-18-0229.1.

Griffies, S. M., and Coauthors, 2016: OMIP contribution to CMIP6: Experimental and diagnostic protocol for the physical component of the Ocean Model Intercomparison Project. *Geosci. Model Dev.*, **9**, 3231–3296, https://doi.org/10.5194/gmd-9-3231-2016.

Hersbach, H., and Coauthors, 2020: The ERA5 global reanalysis. *Quart. J. Roy. Meteor. Soc.*, **146**, 1999–2049, https://doi.org/10.1002/qj.3803.

Heywood, K. J., and Coauthors, 2014: Ocean processes at the Antarctic continental slope. *Philos. Trans. Roy. Soc.*, **A372**, 20130047, https://doi.org/10.1098/rsta.2013.0047.

——, and Coauthors, 2016: Between the devil and the deep blue sea: The role of the Amundsen Sea continental shelf in exchanges between ocean and ice shelves. *Oceanography*, **29**, 118–129, https://doi.org/10.5670/oceanog.2016.104.

Holland, P. W., and R. E. Welsch, 1997: Robust regression using iteratively reweighted least-squares. *Commun. Stat. Theory Methods*, **A6**, 813–827.

Howard, L. N., 1961: Note on a paper of John W. Miles. *J. Fluid Mech.*, **10**, 509–512, https://doi.org/10.1017/S0022112061000317.

Jacobs, S. S., and C. F. Giulivi, 1985: Interannual ocean and sea ice variability in the Ross Sea. *Ocean, Ice and Atmosphere: Interactions at the Antarctic Continental Margin*, S. Jacobs and R. Weiss, Eds., Antarctic Research Series, Vol. 75, Amer. Geophys. Union, 135–150, https://doi.org/10.1029/AR075p0135.

Jerlov, N. G., 1968: *Optical Oceanography*. Vol. 5. Elsevier, 199 pp.

Jones, R. W., I. A. Renfrew, A. Orr, B. G. M. Webber, D. M. Holland, and M. A. Lazzara, 2016: Evaluation of four global reanalysis products using in situ observations in the Amundsen Sea embayment, Antarctica. *J. Geophys. Res. Atmos.*, **121**, 6240–6257, https://doi.org/10.1002/2015JD024680.

Jourdain, N. C., P. Mathiot, N. Merino, G. Durand, J. Le Sommer, P. Spence, P. Dutrieux, and G. Madec, 2017: Ocean circulation and sea-ice thinning induced by melting ice shelves in the Amundsen Sea. *J. Geophys. Res. Oceans*, **122**, 2550–2573, https://doi.org/10.1002/2016JC012509.

Kim, I., D. Hahm, T. S. Rhee, T. W. Kim, C.-S. Kim, and S. Lee, 2016: The distribution of glacial meltwater in the Amundsen Sea, Antarctica, revealed by dissolved helium and neon. *J. Geophys. Res. Oceans*, **121**, 1654–1666, https://doi.org/10.1002/2015JC011211.

Lazarevich, P., T. Rossby, and C. Mcneil, 2004: Oxygen variability in the near-surface waters of the northern North Atlantic: Observations and a model. *J. Mar. Res.*, **62**, 663–683, https://doi.org/10.1357/0022240042387547.

Lüpkes, C., and G. Birnbaum, 2005: Surface drag in the Arctic marginal sea-ice zone: A comparison of different parameterisation concepts. *Bound.-Layer Meteor.*, **117**, 179–211, https://doi.org/10.1007/s10546-005-1445-8.

Macdonald, G. J., S. F. Ackley, A. M. Mestas-Nuñez, and A. Blanco-Cabanillas, 2023: Evolution of the dynamics, area, and ice production of the Amundsen Sea Polynya, Antarctica, 2016–2021. *Cryosphere*, **17**, 457–476, https://doi.org/10.5194/tc-17-457-2023.

Mankoff, K. D., S. S. Jacobs, S. M. Tulaczyk, and S. E. Stammerjohn, 2012: The role of Pine Island Glacier ice shelf basal channels in deep-water upwelling, polynyas and ocean circulation in Pine Island Bay, Antarctica. *Ann. Glaciol.*, **53**, 123–128, https://doi.org/10.3189/2012AoG60A062.

Martin, S., and P. Kauffman, 1981: A field and laboratory study of wave damping by grease ice. *J. Glaciol.*, **27**, 283–313, https://doi.org/10.3189/S0022143000015392.

Martinson, D. G., 1990: Evolution of the Southern Ocean winter mixed layer and sea ice: Open ocean deepwater formation and ventilation. *J. Geophys. Res.*, **95**, 11 641–11 654, https://doi.org/10.1029/JC095iC07p11641.

Maykut, G. A., 1978: Energy exchange over young sea ice in the central Arctic. *J. Geophys. Res.*, **83**, 3646–3658, https://doi.org/10.1029/JC083iC07p03646.

——, 1982: Large-scale heat exchange and ice production in the central Arctic. *J. Geophys. Res.*, **87**, 7971–7984, https://doi.org/10.1029/JC087iC10p07971.

McDougall, T. J., and P. M. Barker, 2011: Getting started with TEOS-10 and the Gibbs Seawater (GSW) oceanographic toolbox. SCOR/IAPSO WG 127, 34 pp., https://www.teos-10.org/pubs/Getting_Started.pdf.

Meneghello, G., J. Marshall, J.-M. Campin, E. Doddridge, and M.-L. Timmermans, 2018: The ice-ocean governor: Ice-ocean stress feedback limits Beaufort gyre spin-up. *Geophys. Res. Lett.*, **45**, 11 293–11 299, https://doi.org/10.1029/2018GL080171.

Miles, J. W., 1961: On the stability of heterogeneous shear flows. *J. Fluid Mech.*, **10**, 496–508, https://doi.org/10.1017/S0022112061000305.

Nihashi, S., and K. I. Ohshima, 2015: Circumpolar mapping of Antarctic coastal polynyas and landfast sea ice: Relationship and variability. *J. Climate*, **28**, 3650–3670, https://doi.org/10.1175/JCLI-D-14-00369.1.

——, ——, and T. Tamura, 2017: Sea-ice production in Antarctic coastal polynyas estimated from AMSR2 data and its validation using AMSR-E and SSM/I-SSMIS data. *IEEE J. Sel. Top. Appl. Earth Obs. Remote Sens.*, **10**, 3912–3922, https://doi.org/10.1109/JSTARS.2017.2731995.

Photopoulou, T., M. A. Fedak, J. Matthiopoulos, B. McConnell, and P. Lovell, 2015: The generalized data management and collection protocol for Conductivity-Temperature-Depth Satellite Relay Data Loggers. *Anim. Biotelemetry*, **3**, 21, https://doi.org/10.1186/s40317-015-0053-8.

Price, J. F., R. A. Weller, and R. Pinkel, 1986: Diurnal cycling: Observations and models of the upper ocean response to diurnal heating, cooling and wind mixing. *J. Geophys. Res.*, **91**, 8411–8427, https://doi.org/10.1029/JC091iC07p08411.

Randall-Goodwin, E., and Coauthors, 2015: Freshwater distributions and water mass structure in the Amundsen Sea Polynya region, Antarctica. *Elementa*, **3**, 000065, https://doi.org/10.12952/journal.elementa.000065.

Roquet, F., and Coauthors, 2013: Estimates of the Southern Ocean general circulation improved by animal-borne instruments. *Geophys. Res. Lett.*, **40**, 6176–6180, https://doi.org/10.1002/2013GL058304.

——, and Coauthors, 2014: A Southern Indian Ocean database of hydrographic profiles obtained with instrumented elephant seals. *Sci. Data*, **1**, 140028, https://doi.org/10.1038/sdata.2014.28.

Saenz, B. T., D. C. McKee, S. C. Doney, D. G. Martinson, and S. E. Stammerjohn, 2023: Influence of seasonally varying sea-ice concentration and subsurface ocean heat on sea-ice thickness and sea-ice seasonality for a 'warm-shelf' region in

Antarctica. *J. Glaciol.*, **69**, 1466–1482, https://doi.org/10.1017/jog.2023.36.

St-Laurent, P., P. L. Yager, R. M. Sherrell, S. E. Stammerjohn, and M. S. Dinniman, 2017: Pathways and supply of dissolved iron in the Amundsen Sea (Antarctica). *J. Geophys. Res. Oceans*, **122**, 7135–7162, https://doi.org/10.1002/2017JC013162.

Tamura, T., K. I. Ohshima, and S. Nihashi, 2008: Mapping of sea ice production for Antarctic coastal polynyas. *Geophys. Res. Lett.*, **35**, L07606, https://doi.org/10.1029/2007GL032903.

——, ——, A. D. Fraser, and G. D. Williams, 2016: Sea ice production variability in Antarctic coastal polynyas. *J. Geophys. Res. Oceans*, **121**, 2967–2979, https://doi.org/10.1002/2015JC011537.

Wadhams, P., G. Aulicino, F. Parmiggiani, P. O. G. Persson, and B. Holt, 2018: Pancake ice thickness mapping in the Beaufort Sea from wave dispersion observed in SAR imagery. *J. Geophys. Res. Oceans*, **123**, 2213–2237, https://doi.org/10.1002/2017JC013003.

Wåhlin, A. K., O. Kalén, K. M. Assmann, E. Darelius, H. K. Ha, T. W. Kim, and S. H. Lee, 2016: Subinertial oscillations on the Amundsen Sea shelf, Antarctica. *J. Phys. Oceanogr.*, **46**, 2573–2582, https://doi.org/10.1175/JPO-D-14-0257.1.

Webber, B. G. M., and Coauthors, 2017: Mechanisms driving variability in the ocean forcing of Pine Island Glacier. *Nat. Commun.*, **8**, 14507, https://doi.org/10.1038/ncomms14507.

Wilson, E. A., S. C. Riser, E. C. Campbell, and A. P. S. Wong, 2019: Winter upper-ocean stability and ice–ocean feedbacks in the sea ice–covered Southern Ocean. *J. Phys. Oceanogr.*, **49**, 1099–1117, https://doi.org/10.1175/JPO-D-18-0184.1.

Xu, Y., W. G. Zhang, T. Maksym, R. Ji, and Y. Li, 2023: Stratification breakdown in Antarctic coastal polynyas. Part I: Influence of physical factors on the destratification time scale. *J. Phys. Oceanogr.*, **53**, 2047–2067, https://doi.org/10.1175/JPO-D-22-0218.1.

Yager, P. L., and Coauthors, 2012: ASPIRE: The Amundsen Sea Polynya international research expedition. *Oceanography*, **25**, 40–53, https://doi.org/10.5670/oceanog.2012.73.

Yang, H. W., and Coauthors, 2022: Seasonal variability of ocean circulation near the Dotson Ice Shelf, Antarctica. *Nat. Commun.*, **13**, 1138, https://doi.org/10.1038/s41467-022-28751-5.

Zheng, Y., K. J. Heywood, B. G. M. Webber, D. P. Stevens, L. C. Biddle, L. Boehme, and B. Loose, 2021: Winter seal-based observations reveal glacial meltwater surfacing in the southeastern Amundsen Sea. *Commun. Earth Environ.*, **2**, 40, https://doi.org/10.1038/s43247-021-00111-z.